THE SXDF-ALMA 2 arcmin2 DEEP SURVEY

The Astrophysical Journal, 833:195 (9pp), 2016 December 20 doi:10.3847/1538-4357/833/2/195

THE SXDF-ALMA 2 arcmin^2 DEEP SURVEY: STACKING REST-FRAME NEAR-INFRARED SELECTED OBJECTS

Wei-Hao Wang[1,2], Kotaro Kohno[3,4], Bunyo Hatsukade[5,20], Hideki Umehata[3,6], Itziar Aretxaga[7], David Hughes[7], Karina I. Caputi[8], James S. Dunlop[9], Soh Ikarashi[8], Daisuke Iono[5,10], Rob J. Ivison[6,9], Minju Lee[5,11], Ryu Makiya[12,13], Yuichi Matsuda[5,10], Kentaro Motohara[3], Kouichiro Nakanish[5,10], Kouji Ohta[14], Ken-ichi Tadaki[15], Yoichi Tamura[3], Tadayuki Kodama[5,10], Wiphu Rujopakarn[12,16], Grant W. Wilson[17], Yuki Yamaguchi[3], Min S. Yun[17], Jean Coupon[18], Bau-Ching Hsieh[1], and Sébastien Foucaud[19]

[1] Academia Sinica Institute of Astronomy and Astrophysics (ASIAA), No. 1, Sec. 4, Roosevelt Rd., Taipei 10617, Taiwan
[2] Canada–France–Hawaii Telescope (CFHT), 65-1238 Mamalahoa Hwy., Kamuela, HI 96743, USA
[3] Institute of Astronomy, University of Tokyo, 2-21-1 Osawa, Mitaka, Tokyo 181-0015, Japan
[4] Research Center for the Early Universe, The University of Tokyo, 7-3-1 Hongo, Bunkyo, Tokyo 113-0033, Japan
[5] National Astronomical Observatory of Japan (NAOJ), 2-21-1 Osawa, Mitaka, Tokyo 181-8588, Japan
[6] European Southern Observatory, Karl-Schwarzschild-Str. 2, D-85748 Garching, Germany
[7] Instituto Nacional de Astrofísica, Óptica y Electrónica (INAOE), Luis Enrique Erro 1, Sta. Ma. Tonantzintla, Puebla, Mexico
[8] Kapteyn Astronomical Institute, University of Groningen, P.O. Box 800, 9700AV Groningen, The Netherlands
[9] Institute for Astronomy, University of Edinburgh, Royal Observatory, Edinburgh EH9 3HJ, UK
[10] SOKENDAI (The Graduate University for Advanced Studies), 2-21-1 Osawa, Mitaka, Tokyo 181-8588, Japan
[11] Department of Astronomy, The University of Tokyo, 7-3-1 Hongo, Bunkyo-ku, Tokyo 133-0033, Japan
[12] Kavli Institute for the Physics and Mathematics of the Universe, Todai Institutes for Advanced Study, the University of Tokyo, Kashiwa, 277-8583 (Kavli IPMU, WPI), Japan
[13] Max-Planck-Institut für Astrophysik (MPA), Karl-Schwarzschild Str. 1, D-85741 Garching, Germany
[14] Department of Astronomy, Kyoto University, Kyoto 606-8502, Japan
[15] Max-Planck-Institut für extraterrestrische Physik (MPE), Giessenbachstrasse, D-85748 Garching, Germany
[16] Department of Physics, Faculty of Science, Chulalongkorn University, 254 Phayathai Rd., Pathumwan, Bangkok 10330, Thailand
[17] Department of Astronomy, University of Massachusetts, Amherst, MA 01003, USA
[18] Astronomical Observatory of the University of Geneva, ch. d'Ecogia 16, CH-1290 Versoix, Switzerland
[19] Center for Astronomy & Astrophysics, Department of Physics & Astronomy, Shanghai JiaoTong University, 800 Dongchuan Rd., Shanghai 200240, China
Received 2016 June 26; revised 2016 September 20; accepted 2016 September 27; published 2016 December 16

ABSTRACT

We present stacking analyses on our ALMA deep 1.1 mm imaging in the Subaru/*XMM-Newton* Deep Survey Field using 1.6 and 3.6 μm selected galaxies in the CANDELS WFC3 catalog. We detect a stacked flux of $\sim$0.03–0.05 mJy, corresponding to $L_{\rm IR} < 10^{11}\,L_{\odot}$ and a star formation rate (SFR) of $\sim$15 $M_{\odot}$ yr^{-1} at $z = 2$. We find that galaxies that are brighter in the rest-frame near-infrared tend to also be brighter at 1.1 mm, and galaxies fainter than $m_{3.6\,\mu{\rm m}} = 23$ do not produce detectable 1.1 mm emission. This suggests a correlation between stellar mass and SFR, but outliers to this correlation are also observed, suggesting strongly boosted star formation or extremely large extinction. We also find tendencies that redder galaxies and galaxies at higher redshifts are brighter at 1.1 mm. Our field contains $z \sim 2.5$ Hα emitters and a bright single-dish source. However, we do not find evidence of bias in our results caused by the bright source. By combining the fluxes of sources detected by ALMA and fluxes of faint sources detected with stacking, we recover a 1.1 mm surface brightness of up to 20.3 $\pm$ 1.2 Jy deg^{-2}, comparable to the extragalactic background light measured by *COBE*. Based on the fractions of optically faint sources in our and previous ALMA studies and the *COBE* measurements, we find that approximately half of the cosmic star formation may be obscured by dust and missed by deep optical surveys. Much deeper and wider ALMA imaging is therefore needed to better constrain the obscured cosmic star formation history.

Key words: cosmic background radiation – galaxies: evolution – galaxies: high-redshift – submillimeter: galaxies

1. INTRODUCTION

The extragalactic background light (EBL) is a measure of the radiative energy production from star formation and black hole accretion throughout the history of the universe. It is now known that the optical and far-infrared (FIR) portions of the EBL have comparable integrated strengths (e.g., Dole et al. 2006), implying that a large amount of the rest-frame UV radiation is absorbed by dust and reradiated in the FIR. In order to understand the star formation history and accretion history fully, it is thus crucial to map the high-redshift dusty galaxies that give rise to the FIR EBL.

Numerous deep imaging surveys have been carried out in the millimeter and submillimeter (mm/submm) from the ground and in the FIR from space to detect and study the FIR sources (see Casey et al. 2014 and Lutz 2014 for recent reviews). However, because of the effect of confusion on single-dish telescopes, the vast majority of the detected objects have infrared luminosities well above $10^{12}\,L_{\odot}$, corresponding to the bright end of the infrared luminosity functions. In the mm/submm, typically only 10%–40% of the EBL is resolved into discrete bright sources by bolometer array cameras (e.g., Barger et al. 1999; Borys et al. 2003; Greve et al. 2004; Wang et al. 2004; Coppin et al. 2006; Weiß et al. 2009; Scott et al. 2010; Hatsukade et al. 2011). In the FIR, *Herschel* SPIRE surveys are only able to directly resolve $\sim$15% of the 200–500 μm EBL into bright sources (e.g., Oliver et al. 2010). Imaging surveys in strong lensing clusters can nearly fully resolve the mm/submm EBL (e.g., Cowie

[20] NAOJ Fellow.

et al. 2002; Smail et al. 2002; Knudsen et al. 2008; Chen et al. 2013) and provide valuable insight into the nature of the faint sources (Chen et al. 2014). However, the sample sizes for the lensed faint sources remain extremely small.

The advent of ALMA is transforming studies of mm/submm sources. ALMA not only provides a powerful means of following up the single-dish sources, but also serves as a survey machine. In particular, ALMA has the combination of high angular resolution and high sensitivity, the two key elements required to detect faint galaxies beyond the confusion limits of single-dish telescopes. In early ALMA cycles, various small-scale continuum surveys have been conducted (e.g., Umehata et al. 2015; Dunlop et al. 2016, hereafter D16). However, because of the limited observing time, even these ALMA surveys did not reach the sensitivity required to fully resolve the EBL over large areas. Sources detected in these ALMA surveys typically account for ∼40% of the EBL (e.g., Hatsukade et al. 2016, hereafter H16; D16) and the majority of the dusty galaxies remain undetected. One way to break through the current sensitivity limit is, instead of relying on contiguous ALMA mosaic surveys, to exploit the archived data where the individual pointings are sufficiently deep and to look for serendipitously detected faint objects (Hatsukade et al. 2013; Ono et al. 2014; Carniani et al. 2015; Fujimoto et al. 2016; hereafter F16; Oteo et al. 2016). Another way is to employ stacking analyses to obtain averaged mm/submm properties of high-redshift galaxies (e.g., Decarli et al. 2014; Scoville et al. 2014, D16). Here we take the second approach and present stacking analyses of near-infrared (NIR) selected galaxies in our ALMA 1.1 mm survey in the Subaru/*XMM-Newton* Deep Survey Field (SXDF; Furusawa et al. 2008).

Our SXDF-ALMA survey covers an area of 2.0 arcmin^2 within the footprint of the Cosmic Assembly Near-IR Deep Extragalactic Legacy Survey (CANDELS; Grogin et al. 2011; Koekemoer et al. 2011) in the SXDF. The extremely deep *HST* WFC3 images provide large numbers of faint, NIR-selected, high-redshift galaxies for stacking analyses. In Section 2, we describe the ALMA and multi-wavelength data. In Section 3, we describe the method of our stacking analyses and the results. In Section 4, we first examine whether a bright, 1.1 mm, single-dish source in our field biases our measurements. We then estimate the contribution to the 1.1 mm EBL from the NIR and ALMA-detected objects, compare our results with previous studies, and discuss the implication. All magnitudes are given in the AB system, where $m_{\rm AB} = 8.9–2.5\log(F)$ when flux F is in units of Jansky. When we compare our 1.1 mm results with previous 1.3 mm and 870 μm results, we assume $F_{1.1\,\rm mm} = 1.65 \times F_{1.3\,\rm mm}$ (F16) and $F_{1.1\,\rm mm} = F_{870\,\mu\rm m}/2.5$ (Oteo et al. 2016).

2. DATA

2.1. SXDF-ALMA Survey

The observations of the SXDF-ALMA Survey (Program ID: 2012.1.00756.S; PI: K. Kohno) and the data reduction will be described in K. Kohno et al. (2016, in preparation; also see Kohno et al. 2016). Here we provide a brief summary and present the ALMA image in Figure 1 (left). We conducted Band 6 (1.1 mm, or 274 GHz) continuum imaging in the SXDF in ALMA Cycle 1, with a 19-point mosaic, a total bandwidth of 7.5 GHz, and a total observing time of 3.6 hr. The field is selected to cover a bright AzTEC 1.1 mm source and 12 $z \sim 2.5$ Hα-selected star-forming galaxies (e.g., Tadaki et al. 2013). The calibration and imaging are performed with the Common Astronomy Software Application package (McMullin et al. 2007). The visibility data were naturally weighted to produce a CLEANed map with a synthesized beam of $0\farcs53 \times 0\farcs41$ (PA = 64°). In this work, we only consider the deep region where the effective coverage is greater than 75% of the peak primary beam response, indicated by the contours in Figure 1. This excludes a bright object near the map edge (SXDF-ALMA 3 in Yamaguchi et al. 2016). The area in this region is 1.58 arcmin^2 and the typical rms noise is 62 μJy beam^{-1}. There are 16 sources detected in this area at $>4\sigma$, and eight sources at $>4.5\sigma$. Up to one-third of the $>4\sigma$ sources could be spurious, based on the number of negative peaks (H16), and the number of spurious sources decreases to zero at $>4.7\sigma$.

2.2. Optical and NIR Data

Our stacking analyses are based on the WFC3 detected objects in the CANDELS catalog of Galametz et al. (2013). This catalog includes *Spitzer* IRAC fluxes of the WFC3 objects, extracted from the images of the *Spitzer* Extended Deep Survey (SEDS; Ashby et al. 2013) at the positions of the WFC3 sources (see Galametz et al. 2013 et al. for details). In Section 3.3 we will show that the IRAC fluxes trace faint 1.1 mm emission better than the WFC3 fluxes, and therefore the majority of our analyses will be based on an additional 3.6 μm selection in the CANDELS catalog. The 5 σ limiting magnitudes in our ALMA area for the *F*160*W* and IRAC 3.6 μm bands are approximately 27.0 and 25.3, respectively. The IRAC fluxes were extracted at the WFC3 positions, so objects can be assigned IRAC fluxes much fainter than the nominal detection limits. but with low S/N. In this work, we consider objects fainter than $m_{3.6\,\mu\rm m} = 26.0$ to be undetected at 3.6 μm. Our visual inspection of the IRAC images does not find any IRAC objects that are undetected by WFC3 (Figure 1 (right)). Therefore, our 3.6 μm selection from the WFC3 pre-selected catalog is not biased against any red objects.

There are 346 CANDELS objects in the 1.58 arcmin^2 area of our ALMA image, among which 151 of them have $>5\sigma$ fluxes at 3.6 μm and 197 of them have $m_{3.6\,\mu\rm m} < 26.0$. We adopt a $0\farcs5$ search radius (approximately the beam FWHM) for our counterpart identification in this work. Among the eight $>4.5\sigma$ ALMA sources, four have CANDELS counterparts. They are discussed in more detail in Yamaguchi et al. (2016). The other four $>4.5\sigma$ ALMA sources have 1.1 mm fluxes of 0.22–0.32 mJy. These eight sources are not included in most of our stacking analyses, but they are included in our analyses of the EBL contribution (Section 4.2). In the 4σ–4.5σ range, there are eight ALMA sources, and only one has a CANDELS counterpart. This implies either a high spurious rate at 4σ–4.5σ, or an extremely dusty population whose NIR light is extinguished. Our analyses in H16 indicate a spurious fraction of $\lesssim$40%. This leaves roughly four real sources that are highly obscured in the optical and rest-frame NIR.

We supplement the CANDELS NIR catalog with our own photometric redshifts. The optical to 4.5 μm data used for our photometric redshifts are similar to those included in the Galametz et al. catalog, except that we also use the *Galex* NUV data and our own CFHT MegaCam *U*-band data obtained in a multi-year *U*-band imaging campaign for the SXDF (W.-H. Wang 2016, in preparation). The photometric redshifts have a

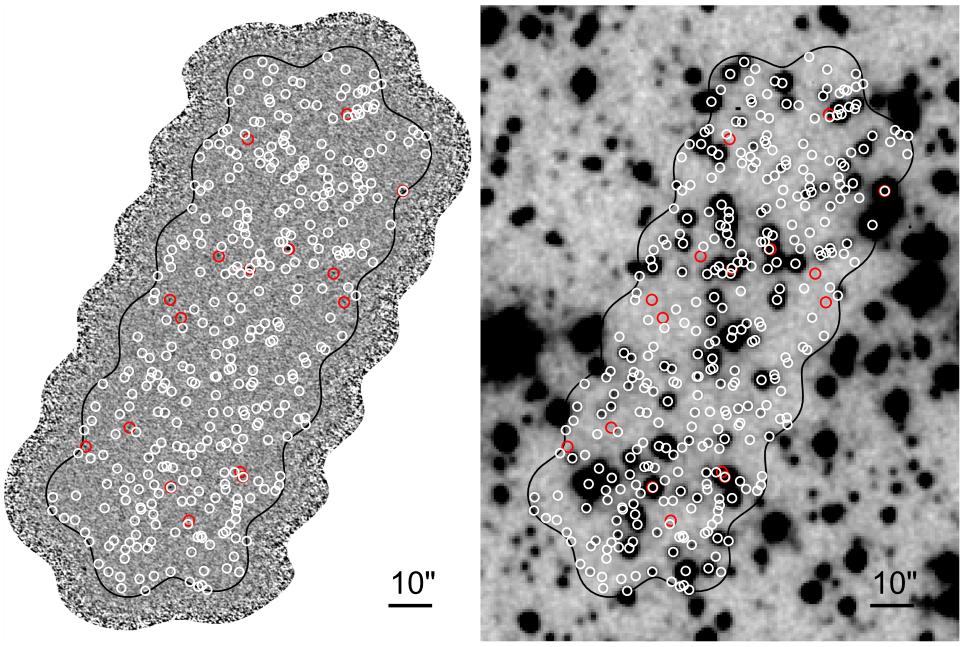

Figure 1. Our ALMA 1.1 mm image (left) and *Spitzer* IRAC 3.6 μm image (right) from the SEDS (Ashby et al. 2013). White circles show the positions of the 346 CANDELS WFC3 objects, and have 1″ radii. Red circles show the $16 > 4\sigma$ ALMA 1.1 mm sources. The area enclosed by the contours has relative weights that are higher than the 75% primary beam response.

very good overall accuracy of$\Delta z/(1+z) = 0.026$ on $K_s < 25.0$ objects. Among the 346 CANDELS objects in the ALMA area, 147 (42%) have reliable photometric redshifts whose χ^2 are sufficiently low. The photometric redshift completeness increases substantially to 89% at $m_{3.6\,\mu\mathrm{m}} < 25.5$. At the bright end of $m_{3.6\,\mu\mathrm{m}} < 23$, 46 out of 53 sources have photometric redshifts after we supplement three photometric redshifts from (Caputi et al. 2011). Nearly all of them are at $z = 0.5$–3.0.

3. STACKING ANALYSES AND RESULTS

3.1. Method

Our stacking analysis method is very similar to those developed by Wang et al. (2012) and To et al. (2014) for Very Large Array images. To avoid biases caused by the small number of brighter objects, we exclude the four NIR objects that are detected at $>4.5\sigma$ by ALMA. We mask them and also the four $>4.5\sigma$ ALMA sources that do not have NIR counterparts in the image. This way, the $>4.5\sigma$ sources do not bias the measured fluxes and noise in our stacking analyses, and our stacking results are more representative of the faint 1.1 mm population. We averaged either the 1.1 mm images centered at the NIR objects or the 1.1 mm fluxes measured at the positions of the NIR objects. Averaging the images and fluxes should give identical results, but the former allows us to examine the image and to examine the average size of the objects. In the stacked image, the mean background, as well as the background rms, can be directly measured. In the flux stacking, we estimated the uncertainties with a Monte Carlo method. We placed random apertures in the image and measured their mean flux. The number of random apertures was identical to the number of NIR sources. There is a finite probability of random apertures being located near bright objects. If their fluxes exceed 4.5σ, they are considered to be "detections" and removed from the random sample, just as we do with the NIR objects. When we estimate the total contribution to the 1.1 mm EBL, we account for these detected sources separately. We repeated this 10^5 times and calculated the mean and standard deviation of the 10^5 mean fluxes. The mean is considered to be a background value and subtracted from the measured mean flux of the NIR selected sources. This statistically removes the effect of faint confusing sources and uncleaned sidelobes. The standard deviation is considered to be the uncertainty in the mean flux of the NIR selected sources. Finally, to test whether our stacking results may be biased, we inserted artificial point sources to the image with random positions. Each time we inserted tens to <200 sources, measured their stacked fluxes, and repeated 10^4 times. We did not find any systematic bias in the average of the 10^4 mean fluxes for input fluxes ranging from 0.005 to 0.2 mJy.

3.2. Results of Image Stacking

We present stacked ALMA 1.1 mm images at the CANDELS 3.6 μm sources in Figure 2. If we simply stack all sources, we do not reach a $>3\sigma$ detection. This indicates that most of the faint 3.6 μm sources do not exhibit strong dust emission. On the other hand, once we split the samples according to their 3.6 μm magnitudes and stack, we see a clear trend that brighter NIR sources are also brighter 1.1 mm sources, on average. This is generally true in all the NIR bands from F125W to 4.5 μm, and the tendency is stronger in the two IRAC bands. We will describe this in more detail in the next subsection. From Figure 2, it can also be seen that the apparent 1.1 mm positions do not always exactly match the NIR positions (circles in the figure). However, the offsets are all smaller than our $\sim$0.″5 ALMA beam in the top four $\Delta m_{3.6\,\mu\mathrm{m}} = 1$ bins. This can be explained with the relatively low S/N. If we stack all sources with $m_{3.6\,\mu\mathrm{m}} < 23$ (lower-right

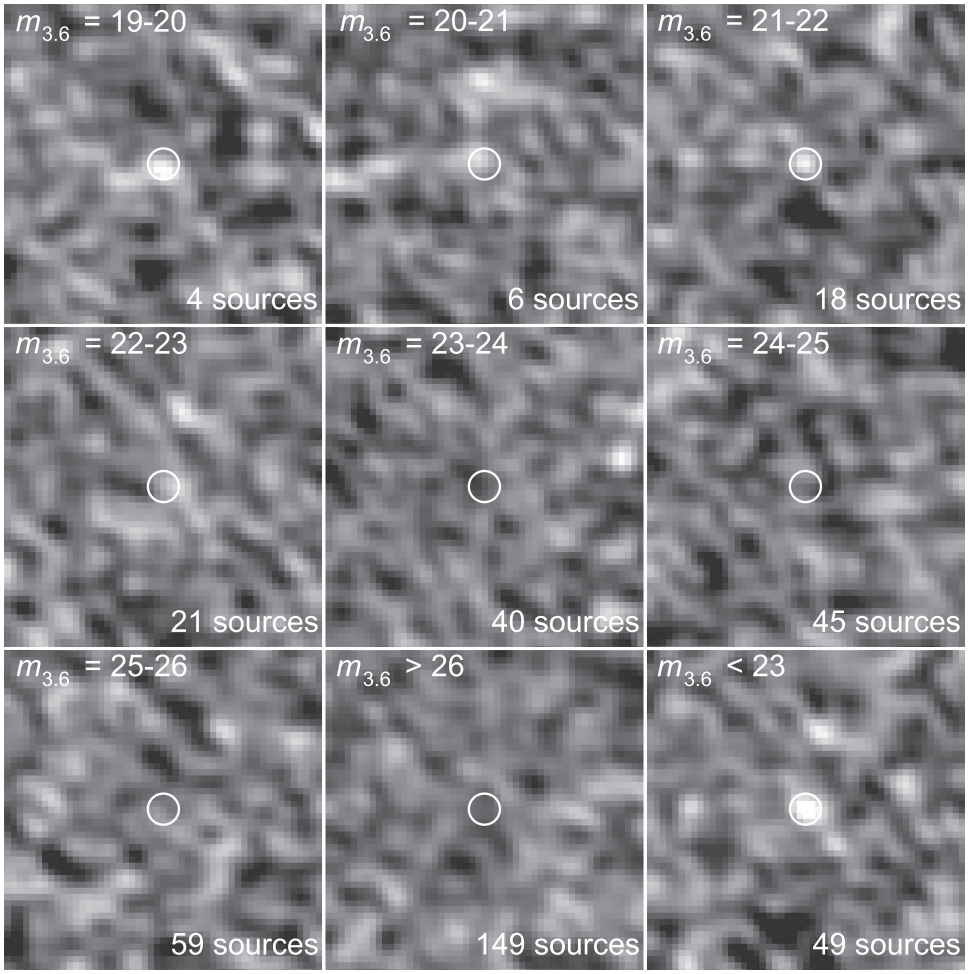

Figure 2. Stacked 1.1 mm images centered at CANDELS WFC3 sources (small circles, $D = 0\farcs5$) in various $m_{3.6\,\mu\mathrm{m}}$ bins. Each panel is 5″ on a side. The brightness scale of each panel is from -2σ to $+4\sigma$. See Table 1 for σ and stacked fluxes. Note that there are $11 > 4\sigma$ ALMA-detected sources without WFC3 counterparts that are therefore not included in any of these panels.

panel of Figure 2, which gives the maximum S/N, the offset disappears.

Our stacked 1.1 mm flux for the 28 $m_{3.6\,\mu\mathrm{m}} < 22$ sources is $\langle F_{1.1\,\mathrm{mm}}\rangle = 0.067 \pm 0.013$ mJy. In Decarli et al. (2014), the stacked 344 GHz for 85 $K < 22$ and $F_{344\,\mathrm{GHz}} < 1.2$ mJy sources is 0.20 ± 0.06 mJy. This is fully consistent with ours once our 1.1 mm stacked flux is scaled by 2.5× (Oteo et al. 2016), given that in this magnitude range, the typical $K - m_{3.6\,\mu\mathrm{m}}$ color is ∼1.0. This is also comparable to the faintest stacked 350 GHz flux reached in Scoville et al. (2014).

We measured the size of detected 1.1 mm emission in the stacked images from the $m_{3.6\,\mu\mathrm{m}} < 23$ bin ($\langle F_{1.1\,\mathrm{mm}}\rangle = 0.050 \pm 0.010$) by fitting a 2D Gaussian distribution. The fitted Gaussian has a FWHM of $0\farcs76 \times 0\farcs43$, slightly larger than the $0\farcs53 \times 0\farcs41$ synthesized beam. This suggests small source sizes that are probably only marginally resolved by the ALMA beam. This is consistent with higher angular resolution ALMA studies of brighter sources (Ikarashi et al. 2015; Simpson et al. 2015) and also the stacking analyses in D16. However, given the low S/N and the apparent offsets between the NIR positions and the stacked 1.1 mm positions in Figure 2, we do not think we can place a meaningful constraint on the source size. We only use this result to guide our selection of flux aperture size in our subsequent analyses.

3.3. Results of Flux Stacking

We move on to measure 1.1 mm fluxes at the positions of the CANDELS sources and stack the fluxes. Based on the above-measured source size, we adopted a relatively small flux aperture, $D = 0\farcs5$ (circles in Figure 2). The aperture correction is derived based on the dirty beam, assuming unresolved sources. Such a small aperture gives higher S/N while still enclosing most of the fluxes from unresolved and slightly resolved objects. It does not require different aperture corrections for CLEANed and unCLEANed sources, since the clean and dirty beams only become substantially different at distances greater than FWHM. The major results are summarized in Table 1.

In Figure 3, we present 1.1 mm fluxes of individual galaxies and stacked 1.1 mm fluxes versus magnitudes at U, $F814W$, $F160W$, and 3.6 μm bands. When the 1.1 mm fluxes are ordered according to the U-band magnitudes, we cannot obtain detections with stacking analyses. Some of the brighter 1.1 mm sources are not even detected at U and therefore not included in the U-band stacking analyses. This shows that the unobscured star formation (traced by rest-frame UV) does not strongly correlate with obscured star formation (traced by dust emission at 1.1 mm). On the other hand, as we move to longer wavebands, there is a tendency that objects more luminous in the rest-frame NIR are brighter 1.1 mm sources. This trend is

Table 1
Results of Stacking Analyses

NIR Sample	N	$\langle F_{1.1\,\mathrm{mm}}\rangle$ (mJy)	EBL (Jy deg $^{-2}$)
$m_{3.6\,\mu\mathrm{m}} = 19$–$20$	4	0.131 ± 0.034	1.19 ± 0.31
$m_{3.6\,\mu\mathrm{m}} = 20$–$21$	6	0.072 ± 0.028	0.98 ± 0.38
$m_{3.6\,\mu\mathrm{m}} = 21$–$22$	18	0.052 ± 0.016	2.12 ± 0.65
$m_{3.6\,\mu\mathrm{m}} = 22$–$23$	21	0.029 ± 0.015	1.39 ± 0.70
$m_{3.6\,\mu\mathrm{m}} = 23$–$24$	40	-0.015 ± 0.011	-1.34 ± 0.97
$m_{3.6\,\mu\mathrm{m}} = 24$–$25$	45	-0.001 ± 0.010	-0.10 ± 1.03
$m_{3.6\,\mu\mathrm{m}} = 25$–$26$	59	0.004 ± 0.009	0.59 ± 1.18
$m_{3.6\,\mu\mathrm{m}} > 26$	149	-0.006 ± 0.006	-1.99 ± 3.26
$m_{3.6\,\mu\mathrm{m}} < 23$	49	0.051 ± 0.010	5.67 ± 1.07
$K_s - m_{4.5\,\mu\mathrm{m}} < 0$	18	0.044 ± 0.016	1.79 ± 0.65
$K_s - m_{4.5\,\mu\mathrm{m}} = 0$–$1$	23	0.029 ± 0.014	1.51 ± 0.73
$K_s - m_{4.5\,\mu\mathrm{m}} > 1$	8	0.131 ± 0.024	2.37 ± 0.43
$z = 0$–2	33	0.040 ± 0.012	2.70 ± 0.80
$z = 2$–4	13	0.097 ± 0.019	2.86 ± 0.56

Note. All the values listed here do not include the four $>4.5\sigma$ ALMA-detected sources. The color and redshift subsamples only include $m_{3.6\,\mu\mathrm{m}} < 23$ objects.

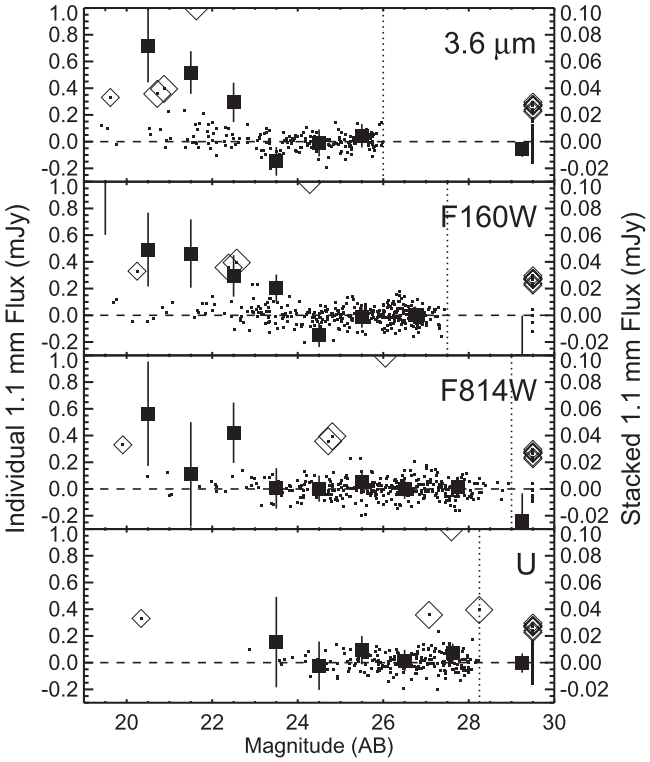

Figure 3. 1.1 mm flux vs. U, $F814W$, $F160W$, and 3.6 μm magnitudes. The small symbols and left-hand y-axis represent fluxes of individual objects. The large filled squares with error bars and the right-hand y-axis represent stacked fluxes in $\Delta m = 1$ bins. Large diamonds are individually detected $>4.5\sigma$ sources and are not included in the stacking analyses. Small diamonds are 4σ–4.5σ sources. Vertical dotted lines show the detection limits at U to 3.6 μm. Objects not detected in these bands are shown at $m = 29.5$ and their stacked fluxes are shown at $m = 29.25$. The stacked results of the brightest $F160W$ and 3.6 μm bins are outside the range of the plots (see Figure 4 for the 3.6 μm one).

the strongest at 3.6 μm. This is consistent with the results in Figure 2. The strong correlation between 3.6 μm magnitudes and stacked 1.1 mm fluxes can be explained by a correlation between stellar mass and obscured star formation. On the other hand, ongoing star formation can also boost the rest-frame NIR luminosity of galaxies and lead to a correlation between 3.6 μm and 1.1 mm. However, this effect should be even stronger in the optical bands (U and $F814W$ in Figure 3), as young stellar populations are blue, and this effect is not observed. Stronger dust extinction in the bright end may hinder this effect in the optical, but the lack of correlation between 3.6 μm magnitudes and galaxy colors in the optical (which should be more strongly affected by extinction) in our samples does not support this scenario. Therefore, a correlation between stellar mass and star formation is a more plausible and natural explanation for the correlation between 3.6 μm and 1.1 mm. This is consistent with the recent results in D16.

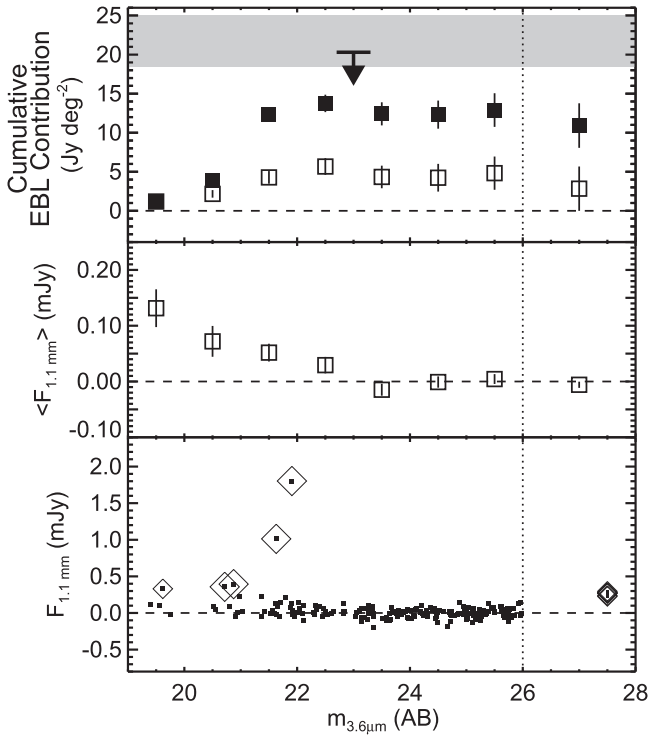

Figure 4. 1.1 mm fluxes and EBL contributions vs. 3.6 μm magnitudes. Bottom panel: 1.1 mm fluxes of individual objects. The four $>4.5\sigma$ detections are enclosed by large open diamonds and they are not included in the subsequent stacking analyses. The 4σ–4.5σ ALMA-detected objects are enclosed by small open diamonds, and are placed at $m_{3.6\,\mu\mathrm{m}} = 27.5$ if they do not have WFC3 counterparts (11 sources). The vertical dotted line shows the 3.6 μm detection limit. Middle panel: stacked flux and flux error in each $\Delta m_{3.6\,\mu\mathrm{m}} = 1$ bin. Top panel: cumulative contribution to the EBL from the NIR selected objects. The open squares show the contribution from $<4.5\sigma$ fluxes. The solid squares show the contribution from all NIR-selected objects (i.e., including the four open diamonds in the bottom panel). We do not show the individual 1.1 mm fluxes of WFC3 objects undetected at 3.6 μm (149 objects), and place their stacked flux and EBL contribution at $m_{3.6\,\mu\mathrm{m}} = 27$. The horizontal bar includes the contribution of all $>4.0\sigma$ ALMA sources and this is an upper limit (see Section 4.2). The shaded band shows the range of the 1.1 mm EBL measured by *COBE*.

The observed correlation between $m_{3.6\,\mu\mathrm{m}}$ and stacked 1.1 mm flux is not universal and is probably only applicable to faint mm/submm sources, on average. At least two of the $>4.5\sigma$ detections (two brightest open diamonds in Figure 4) have 1.1 mm fluxes significantly above the correlation. There also exist an additional four $>4.5\sigma$ sources that do not have counterparts in the CANDELS catalog and are therefore not included in Figure 4. They should have $m_{3.6\,\mu\mathrm{m}} > 26$ and thus are also well above the correlation. Either a dramatically boosted star formation rate (SFR) or an extremely large

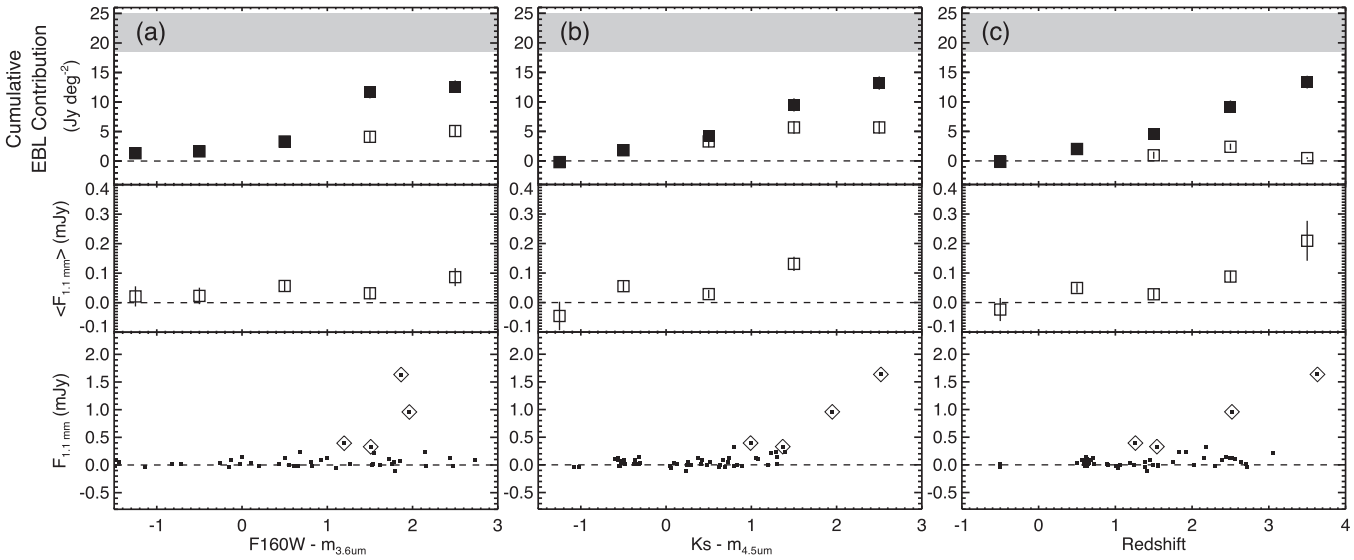

Figure 5. Same as Figure 4, but for 1.1 mm fluxes and EBL contributions vs. $F160W - m_{3.6\,\mu m}$ color (a), vs. $K_s - m_{4.5\,\mu m}$ color (b), and vs. redshift (c), for objects with $m_{3.6\,\mu m} < 23$. ALMA-detected objects (open diamonds) are not included in the stacked fluxes and EBL contributions (open squares). Objects with no reliable photometric redshifts are assigned $z = -0.5$.

extinction rate (or both) can explain these objects. Either of the possibilities should not be surprising for bright mm/submm sources.

In the $m_{3.6\,\mu m} = 20$–22 range, (24 sources) the stacked flux of 0.057 ± 0.014 mJy corresponds to an infrared luminosity of $\sim 9 \times 10^{10}\,L_{\odot}$ for $z = 2$ if we adopt the luminosity-dependent dust spectral energy distribution (SED) in Chary & Elbaz (2001), or $\sim 3\times$ larger if we assume an Arp 220 SED. The SFR derived with the Chary & Elbaz (2001) SED and a Kennicutt (1998) conversion is $\sim 15\,M_{\odot}$ yr^{-1}. The values of infrared luminosity and SFR probed by the $m_{3.6\,\mu m} = 22$–23 stacking samples are $2\times$ smaller, with a lower 2σ significance. The above stacked SFRs should be diluted by an unknown fraction of quiescent galaxies, otherwise the face values are similar to the UV SFR of faint Lyman-break galaxies.

We now focus on stacking analyses based on the 3.6 μm magnitude as it provides the strongest 1.1 mm signal. Figure 4 shows the measured 1.1 mm fluxes versus 3.6 μm magnitudes. Both Figures 3 and 4 show that sources fainter than $m_{3.6\,\mu m} = 23$ do not produce detectable 1.1 mm emission after stacking (except for those ALMA-detected sources without WFC3 counterparts). This does not change if we adopt photometric apertures as large as $2''$, implying that the non-detections are not caused by random positional offsets between the NIR and the 1.1 mm emission.

We estimate the contribution to the 1.1 mm EBL from the stacked objects by dividing their integrated flux with survey area (top panel of Figure 4). At $m_{3.6\,\mu m} < 23$, the cumulative contributions are 5.67 ± 1.07 Jy deg^{-2} from sources with $<4.5\sigma$ ALMA fluxes, and 13.75 ± 1.12 Jy deg^{-2} from all sources. The 1.1 mm EBL measured by the *COBE* FIRAS experiments is 18.5 Jy deg^{-2} (Puget et al. 1996) or 25.1 Jy deg^{-2} (Fixsen et al. 1998). This range of 18.5–25.1 Jy deg^{-2} probably reflects the systematic uncertainty in the measurements, and is shown in the shaded area in the top panel of Figure 4. Our recovered EBL from all $m_{3.6\,\mu m} < 23$ sources corresponds to 60% to 80% of the COBE values. We will discuss this further in Section 4.

We can use stacking analyses to examine the 1.1 mm flux as functions of NIR color on the 49 sources with $m_{3.6\,\mu m} < 23$. In previous studies, it has been shown that bright mm/submm sources tend to be redder in the NIR and IRAC wavebands (e.g., Chen et al. 2016) and likely vice versa (e.g., Wang et al. 2012; Caputi et al. 2014). Figures 5(a) and (b) show that this is also the case for faint sources (also see Table 1). The four $>4.5\sigma$ ALMA sources with NIR counterparts all have moderately red $F160W - m_{3.6\,\mu m}$ colors and extremely red $K_s - m_{4.5\,\mu m}$ colors. The stacked fluxes also suggest a tendency for redder sources to be brighter at 1.1 mm, although this is primarily driven by the sources in the $F160W - m_{3.6\,\mu m} = 2$–$3$ and $K_s - m_{4.5\,\mu m} = 1$–2 bins.

Finally, we present the redshift dependence of the stacked 1.1 mm flux of the 46 sources with redshifts and $m_{3.6\,\mu m} < 23$ in Figure 5(c) (also see Table 1). The diagram remarkably resembles that in Figure 5(b), because the $K_s - m_{4.5\,\mu m}$ color almost monotonically increases with redshift (see, e.g., Figure 1 in Wang et al. 2012) at $z < 3$. Similarly, the trend is primarily driven by the few sources at higher redshifts, and the stacked fluxes of fainter objects are noisy.

4. DISCUSSION

4.1. The Bright AzTEC Source

Our ALMA field is not an unbiased blank field, as it was chosen to include a bright, 3.5 mJy AzTEC source (S. Ikarashi et al. 2016, in preparation). This source splits into two sources under ALMA's resolution (the two brightest sources in the bottom panels of Figures 4 and 5). The total flux of these sources measured by Yamaguchi et al. (2016) is 3.4 ± 0.18 mJy, consistent with the AzTEC flux. They both show an excess of emission in the 2315 nm narrowband filter (Tadaki et al. 2015), suggesting an Hα redshift of $z = 2.53$. This redshift is consistent with their photometric redshifts (Yamaguchi et al. 2016), given the large photometric redshift errors, but needs to be confirmed with spectroscopy. We expect to enclose $\sim$0.1 such objects in our ALMA field, based on its AzTEC flux and the blank field AzTEC counts in Scott et al.

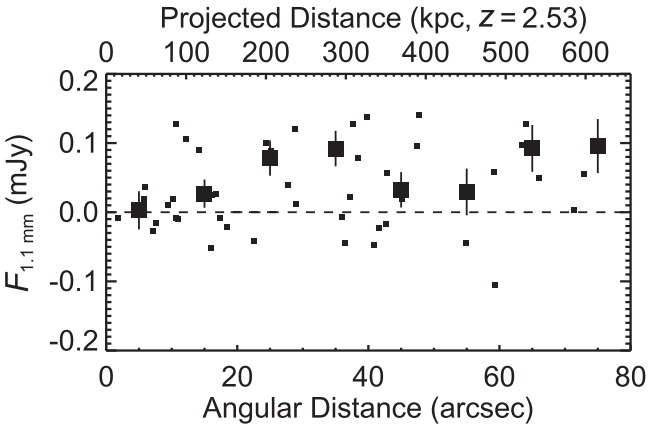

Figure 6. 1.1 mm fluxes of $m_{3.6\,\mu m} < 23$ galaxies vs. the projected distance from the bright AzTEC source (measured from the center of the two bright ALMA sources). Small symbols are individual fluxes, and solid squares with error bars are stacked fluxes. The top x-axis is the projected physical distance at $z = 2.53$, the Hα redshift of the two bright ALMA sources.

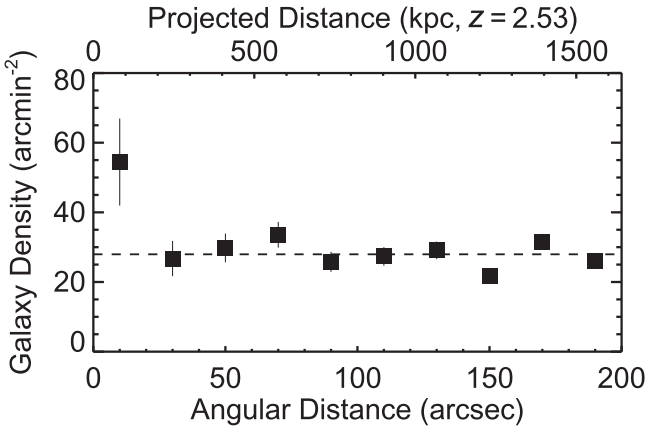

Figure 7. Similar to Figure 6 but for the surface density of $m_{3.6\,\mu m} < 23$ galaxies. The error bars are Poisson errors in the galaxy counts.

(2012), if our field is randomly placed. From this point of view, it is a rare object and the overdensity associated with it may bias our results. On the other hand, if we look at them individually based on their ALMA fluxes, we expect to find ∼0.3 and ∼0.8 sources in our ALMA field based on the AzTEC counts. In that case, the existence of such sources in our survey may not be too surprising.

Nevertheless, it is possible that our stacking results are biased, especially in the area around the 3.5 mJy AzTEC source. This concern arises from the fact that bright mm/submm sources are strongly clustered and reside in massive dark matter halos (e.g., Hickox et al. 2012; Chen et al. 2016). We can test this with our data. In the ALMA studies of color-selected sources in Decarli et al. (2014), the authors found tentative evidence that galaxies within 200 kpc from bright 870 μm sources tend to also be brighter at 870 μm. We do not detect such a trend for the 3.6 μm sources in our ALMA field. In Figure 6, we show 1.1 mm fluxes versus projected distance from the bright AzTEC source (measured from the center of the two bright ALMA sources) on $m_{3.6\,\mu m} < 23$ objects. We see no evidence of elevated 1.1 mm flux near the bright source within the scales probed by our ALMA imaging. This does not change even if we include fainter 3.6 μm objects. The difference between the results here and those in Decarli et al. (2014) could be caused by sample sizes (one bright AzTEC source here versus >100 LABOCA sources in Decarli et al.).

We also investigate the number density of $m_{3.6\,\mu m} < 23$ galaxies as a function of the projected distance from the bright AzTEC source. The result is shown in Figure 7. There is a 2σ overdensity within 20″ around the bright AzTEC source. This overdensity can be observed until $m_{3.6\,\mu m} < 24$, and then the area becomes underdense in $24 < m_{3.6\,\mu m} < 26$. The combined density distribution becomes more or less flat for all galaxies with $m_{3.6\,\mu m} < 26$. Moreover, using the photometric redshifts (∼30% complete at $m_{3.6\,\mu m} < 26$), we found that galaxies with photometric redshifts of <2.0 contribute 21 ± 10 arcmin^{-2} to the surface density above the large-scale average at $r < 20''$. The overdensity at $r < 20''$ in Figure 7 is thus primarily driven by galaxies unrelated to the AzTEC source, and is probably a result of small number statistics. We conclude that there is no solid evidence of overdensity around the bright AzTEC source. Even if the overdensity in Figure 7 is real, after being multiplied by the low stacked flux shown in Figure 6, it does not alter our results of mean 1.1 mm fluxes of galaxies or the EBL contribution. In our discussion below, we do not make special treatments for galaxies near the AzTEC source. However, we consider results derived with and without the two bright ALMA sources that compose of the AzTEC source.

4.2. Resolved EBL

A key question we would like to address with our SXDF-ALMA survey is how much of the 1.1 mm EBL can be directly detected (see H16) and recovered with stacking analyses. An EBL contribution of 13.75 ± 1.12 Jy deg^{-2} is recovered if we include all NIR sources, which is shown by the solid squares in the top panel of Figure 4. We can further include ALMA-detected sources without NIR counterparts (i.e., not included in the stacking analyses). The results are 16.1 ± 1.2 Jy deg^{-2} and 20.3 ± 1.2 Jy deg^{-2}, respectively, for including $>4.5\sigma$ and $>4\sigma$ sources. The latter is the downward pointing arrow in the top panel of Figure 4 and the upper end of the solid box in Figure 8. All these values are upper limits for the following reasons. First, our ALMA field is chosen to include a bright AzTEC source. Based on the blank-field counts in Scott et al. (2012), we expect <1 such sources in our ALMA field, whether for a single, bright AzTEC source or for the two ALMA sources that it splits into. Second, between 4σ and 4.5σ, the combined effect of flux boosting (∼15%–20%), spurious sources ($\lesssim$40%), and completeness (∼70%) may overestimate the contribution in the 4σ–4.5σ interval (H16).

A more direct way to account for all of the above effects is to involve our number counts in H16, which took into account flux boosting, spurious fraction, and completeness. The bright end of the counts in H16 is supplemented by single-dish counts and is not entirely based on the SXDF-ALMA data. The H16 counts fitted with a Schechter function integrated to 0.2 mJy yield an EBL contribution of 9.2 Jy deg^{-2}, which is represented by the thick blue curve in Figure 8. After removing sources already accounted for in H16, our stacked EBL contribution from NIR sources without ALMA detections is 4.9 Jy deg^{-2}. Therefore, the combined EBL contribution from bright and faint sources is 14.1 Jy deg^{-2}. This is the lower end of the solid box in Figure 8. This is comparable with the result in D16, who also employ stacking analyses to supplement the directly detected fluxes.

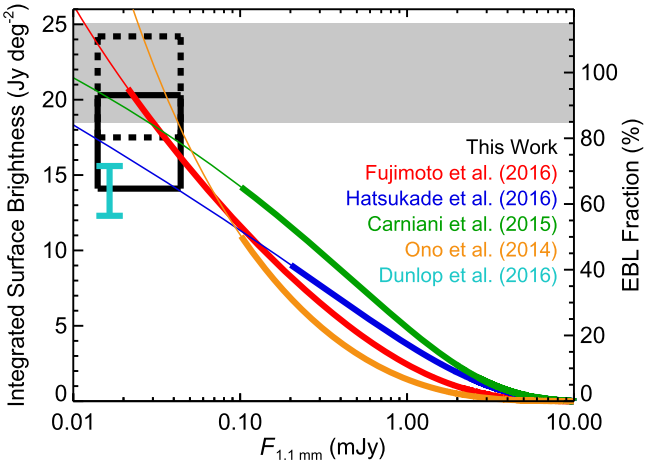

Figure 8. Resolved 1.1 mm EBL. Our stacking analyses plus ALMA-detected sources in the SXDF are shown with the solid box. The top and bottom ends of the box correspond to the upper and lower limits discussed in Section 4.2. The horizontal position and width are the stacked flux and flux errors, respectively, of the NIR sources in the $m_{3.6\,\mu\mathrm{m}} = 22$–$23$ bin. The dashed box includes the contribution from a hypothesized optically faint population discussed in Section 4.3. Color curves show the cumulative EBL contributions derived from Schechter fits to number counts in recent ALMA studies. The thick portions of the curves indicate the flux range probed by these studies and the thin portions are the extrapolations. The cyan error bar is the 1.3 mm result from D16, scaled by 1.65× to 1.1 mm (F16). The shaded band shows the range of the 1.1 mm EBL measured by *COBE*, and the middle point is labeled as 100% along the right-y axis.

The solid box in Figure 8 represents the range of resolved EBL probed by our stacking of faint objects, plus two different treatments of bright objects (total detected flux in our field or adopting the wide-field bright-end counts). It is broadly consistent with that in F16, who conducted the most thorough search by far for serendipitously detected faint continuum sources in deep ALMA 1.2 mm pointings in the archive. The counts in F16 at a >0.02 mJy level lead to an EBL contribution of $22.9^{+6.7}_{-5.6}$ Jy deg^{-2}, while we recover up to 20.3 Jy deg^{-2} of EBL at 1.1 mm with stacking analyses on a faint population with $\langle F_{1.1\,\mathrm{mm}}\rangle \sim 0.03$ mJy. The caveat here is that the F16 sample includes 1.2 mm sources that are optically faint, while our stacked signal comes from relatively bright NIR sources ($m_{3.6\,\mu\mathrm{m}} < 23$). This leads to our next discussion topic.

4.3. Optically Faint Sources

Once we detect the majority of galaxies that give rise to the mm/submm EBL, we would like to ask what kinds of galaxies they are. In addition to the color and redshift distributions of these galaxies, the fraction of optically faint galaxies (i.e., galaxies missed by deep optical/NIR surveys) is of particular interest. This tells us whether the star formation history constructed from optically selected galaxies is representative, or needs significant revision. We can gain insight into this by comparing our results with the results of F16 and with the *COBE* EBL values.

The EBL resolved by our ALMA imaging and stacking analyses is still lower than the EBL measured by *COBE*. This suggests a considerable fraction (anywhere between 0% and 44%) of EBL arising from sources fainter than the CANDELS detection limit. Such extremely optically faint sources have been found in previous surveys (e.g., Wang et al. 2009), as well as our SXDF-ALMA survey (SXDF-ALMA3 in Yamaguchi et al. 2016). They are also hinted at by the large number of ALMA-detected sources without CANDELS counterparts (four out of eight for $F_{1.1\,\mathrm{mm}} > 4.5\sigma$). The optically faint fraction (50%) is similar to that in F16 (41%).

Because of the above, we hypothesize an optically faint population that is not picked up by our NIR selection. We further assume that this population accounts for ∼41% of the EBL from the faint end, based on the optically faint fraction in F16, for its larger sample size and higher ALMA sensitivity. This means there is a completeness correction of $1/(1-0.41)$ for our NIR stacked EBL. Once we do so, the solid box in Figure 8 becomes the dashed box, corresponding to 17.5–24.2 Jy deg^{-2}. This is comparable to the range allowed by the *COBE* measurements and the range probed/extrapolated by previous number counts. We therefore conclude that an optically faint fraction in the ballpark of 50%–60% is consistent with existing data for both the bright and faint ends of the 1.1/1.2 mm population. If this is the case, then optical studies can only account for some 50% of high-redshift star-forming galaxies.

The above studies demonstrate that with existing ALMA data, we just barely can scrape the surface of the issues raised by the resolved EBL and extremely dusty galaxies. Future ALMA deep imaging will be able to put better constraints on the optically faint fraction as functions of mm/submm fluxes. Ultimately, the accuracy in ALMA determinations of the EBL contribution from discrete sources may even exceed that in the *COBE* measurements. These will further transform our understanding of the dusty side of the galaxy evolution.

We thank Seiji Fujimoto for the useful discussion and the referee for the thorough report. W.H.W. was a resident astronomer at the CFHT when the majority of the analyses were carried out. W.H.W. is supported by the Ministry of Science and Technology of Taiwan (102-2119-M-001-007-MY3 and 105-2112-M-001-029-MY3). B.H., Y.T., and Y.M. are supported by the Japan Society for Promotion of Science (JSPS) KAKENHI (Nos. 15K17616, 25103503, 15H02073, 20647268). K.K. is supported by the ALMA Japan Research Grant of NAOJ Chile Observatory, NAOJ-ALMA-0049. K.C. and S.I. acknowledge the support of the Netherlands Organisation for Scientific Research (NWO) through the Top Grant Project 614.001.403. J.S.D. acknowledges the support of the European Research Council via an Advanced Grant. M.L. is financially supported by a Research Fellowship from JSPS for Young Scientists. H.U. acknowledges the support from Grant-in-Aid for JSPS Fellows, 26.11481. This paper makes use of the following ALMA data: ADS/JAO. ALMA#2012.1.00756.S. ALMA is a partnership of ESO (representing its member states), NSF (USA) and NINS (Japan), together with NRC (Canada), NSC and ASIAA (Taiwan), and KASI (Republic of Korea), in cooperation with the Republic of Chile. The Joint ALMA Observatory is operated by ESO, AUI/NRAO and NAOJ. This paper is partially based on observations obtained with MegaPrime/MegaCam, a joint project of CFHT and CEA/DAPNIA, at the CFHT, which is operated by the National Research Council (NRC) of Canada, the Institut National des Sciences de l'Univers of the Centre National de la Recherche Scientifique of France, and the University of Hawaii.

REFERENCES

Ashby, M. L. N., Willner, S. P., Fazio, G. G., et al. 2013, ApJ, 769, 80
Barger, A. J., Cowie, L. L., & Sanders, D. B. 1999, ApJL, 518, L1

Borys, C., Chapman, S., Helpern, M., & Scott, D. 2003, MNRAS, 344, 385
Caputi, K. I., Cirasuolo, M., Dunlop, J. S., et al. 2011, MNRAS, 413, 162
Caputi, K. I., Michałowski, M. J., Krips, M., et al. 2014, ApJ, 788, 126
Carniani, S., Maiolino, R., De Zotti, G., et al. 2015, A&A, 584, 78
Casey, C. M., Narayanan, D., & Cooray, A. 2014, PhR, 541, 45
Chary, R., & Elbaz, D. 2001, ApJ, 556, 562
Chen, C.-C., Cowie, L. L., Barger, A. J., et al. 2013, ApJ, 776, 131
Chen, C.-C., Cowie, L. L., Barger, A. J., Wang, W.-H., & Williams, J. P. 2014, ApJ, 789, 12
Chen, C.-C., Smail, I., Ivison, R. J., et al. 2016, ApJ, 820, 82
Coppin, K., Chapin, E. L., Mortier, A. M. J., et al. 2006, MNRAS, 372, 1621
Cowie, L. L., Barger, A. J., & Kneib, J.-P. 2002, AJ, 123, 2197
Decarli, R., Smail, I., Walter, F., et al. 2014, ApJ, 780, 115
Dole, H., Lagache, G., Puget, J.-L., et al. 2006, A&A, 451, 417
Dunlop, J. S., McLure, R. J., Biggs, A. D., et al. 2016, MNRAS, submitted (arXiv:1606.00227) (D16)
Fixsen, D. J., Dwek, E., Mather, J. C., Bennett, C. L., & Shafer, R. A. 1998, ApJ, 508, 123
Fujimoto, S., Ouchi, M., Ono, Y., et al. 2016, ApJS, 222, 1 (F16)
Furusawa, H., Kosugi, G., Akiyama, M., et al. 2008, ApJS, 176, 1
Galametz, A., Grazian, A., Fontana, A., et al. 2013, ApJS, 206, 10
Greve, T. R., Ivison, R. J., Bertoldi, F., et al. 2004, MNRAS, 354, 779
Grogin, N., Kocevski, D., Faber, S. M., et al. 2011, ApJS, 197, 35
Hatsukade, B., Kohno, K., Aretxaga, I., et al. 2011, MNRAS, 411, 102
Hatsukade, B., Kohno, K., Umehata, H., et al. 2016, PASJ, 68, 36 (H16)
Hatsukade, B., Ohta, K., Seko, A., Yabe, K., & Akiyama, M. 2013, ApJL, 769, L27
Hickox, R. C., Wardlow, J. L., Smail, I., et al. 2012, MNRAS, 421, 284
Ikarashi, S., Ivison, R. J., Caputi, K., et al. 2015, ApJ, 810, 133
Kennicutt, R. C. 1998, ARA&A, 36, 189
Knudsen, K. K., van der Werf, P. P., & Kneib, J.-P. 2008, MNRAS, 384, 1611
Koekemoer, A. M., Faber, S. M., Ferguson, H. C., et al. 2011, ApJS, 197, 36
Kohno, K., Yamaguchi, Y., Tamura, Y., et al. 2016, in Proc. IAU Symp. 319, Galaxies at High Redshift and Their Evolution Over Cosmic Time (Cambridge: Cambridge Univ. Press), 92
Lutz, D. 2014, ARA&A, 52, 373
McMullin, J. P., Waters, B., Schiebel, D., Young, W., & Golap, K. 2007, in ASP Conf. Ser. 376, Astronomical Data Analysis Software and Systems XVI, ed. R. A. Shaw, F. Hill, & D. J. Bell (San Francisco, CA: ASP), 127
Oliver, S. J., Wang, L., Smith, A. J., et al. 2010, A&A, 518, L21
Ono, Y., Ouchi, M., Kurono, Y., & Momose, R. 2014, ApJ, 795, 5
Oteo, I., Zwaan, M. A., Ivison, R. J., Smail, I., & Biggs, A. D. 2016, ApJ, 822, 36
Puget, J.-L., Abergel, A., Bernard, J.-P., et al. 1996, A&A, 308, L5
Scott, K. S., Wilson, G. W., Aretxaga, I., et al. 2012, MNRAS, 423, 575
Scott, K. S., Yun, M. S., Wilson, G. W., et al. 2010, MNRAS, 405, 2260
Scoville, N., Aussel, H., Sheth, K., et al. 2014, ApJ, 783, 84
Simpson, J. M., Smail, I., Swinbank, A. M., et al. 2015, ApJ, 799, 81
Smail, I., Ivison, R. J., Blain, A. W., & Kneib, J.-P. 2002, MNRAS, 331, 495
Tadaki, K., Kodama, T., Tanaka, I., et al. 2013, ApJ, 778, 114
Tadaki, K., Kohno, K., Kodama, T., et al. 2015, ApJL, 811, L3
To, C.-H., Wang, W.-H., & Owen, F. N. 2014, ApJ, 792, 139
Umehata, H., Tamura, Y., Kohno, K., et al. 2015, ApJL, 815, L8
Wang, W.-H., Barger, A. J., & Cowie, L. L. 2009, ApJ, 690, 319
Wang, W.-H., Barger, A. J., & Cowie, L. L. 2012, ApJ, 744, 155
Wang, W.-H., Cowie, L. L., & Barger, A. J. 2004, ApJ, 613, 655
Weiß, A., Kovács, A., Coppin, K., et al. 2009, ApJ, 707, 1201
Yamaguchi, Y., Tamura, Y., Kohno, K., et al. 2016, PASJ, 68, 82